

Probe of the Band Structure of MBE Grown *p*-Type InMnAs at Ultrahigh Magnetic Fields

Y. Sun, F. V. Kyrychenko, G. D. Sanders and C. J. Stanton
Department of Physics, University of Florida
P. O. Box 118440, Gainesville, Florida 32611, USA

G. A. Khodaparast*
Department of Physics, Virginia Tech
Blacksburg, VA 24061, USA
khoda@vt.edu

J. Kono
Department of Electrical and Computer Engineering
Rice University, Houston, Texas 77005, USA

Y. H. Matsuda
Institute for Solid State Physics
University of Tokyo 5-1-5 Kashiwanoha
Kashiwa, Chiba 277-8581, Japan

H. Munekata
Image Science and Engineering Laboratory
Tokyo Institute of Technology
Yokohama, Kanagawa 226-8503

Received 26 December 2014

Accepted 24 February 2015

Published 27 April 2015

We present a theoretical and experimental study on electronic and magneto-optical properties of *p*-type paramagnetic InMnAs dilute magnetic semiconductor (DMS) alloys in ultrahigh (> 100 T) external magnetic fields (\mathbf{B}). Theoretical calculations are based on an 8-band Pidgeon–Brown model which is generalized to include the wavevector dependence of the electronic states along \mathbf{B} as well as *s*–*d* and *p*–*d* exchange interactions with localized Mn *d*-electrons. The spin-dependent electronic structure as a function of Mn doping is computed and the dependence of the valence band structure on parameters such as the *sp*–*d* exchange interaction strength and effective masses in paramagnetic *p*-InMnAs alloys are examined. The cyclotron resonance (CR) and magneto-optical properties of InMnAs are calculated using Fermi’s golden rule. Two strong CR peaks are observed in *p*-type InMnAs alloys which correspond to the transitions within either heavy-hole (HH) or light-hole (LH) Landau levels. Furthermore, we also observed strong resonance absorption for electron-active polarization which can occur in *p*-type semiconductors originating from transitions between the light and heavy hole Landau levels.

*Corresponding author.

Keywords: Ultrahigh magnetic fields; InMnAs; narrow gap semiconductors; cyclotron resonance; ferromagnetic semiconductors.

PACS Number(s): 75.50.Pp, 78.20.Ls, 78.40.Fy.

1. Introduction

Compound semiconductors such as InAs and InSb have unique properties that result from their small effective masses, high electron mobilities, and very large g-factors.¹ There is now a rapidly growing interest in the science and engineering of multifunctional narrow gap semiconductors (NGS) that include magnetic elements such as Mn. But most of the current research activities in the area of magnetic semiconductors, have been focused on III-Mn-V alloys such as GaMnAs,^{2,3} with large valence band effective masses; therefore, it is important in this context to explore the opposite extremes of the III-Mn-V ternaries i.e., InMnAs with smaller effective mass and larger spin-orbit couplings.^{4,5} Probing the bandstructure of In_{1-x}Mn_xAs dilute magnetic semiconductors (DMSs) is important for designing ferromagnetic heterostructures, which may in turn prove useful in the fabrication of spintronic devices.^{2,3,6-11}

Furthermore, carrier-induced ferromagnetism in III-V semiconductors^{8,12,13} and the interaction with the localized spins of magnetic impurities have been studied extensively,^{14,15} but the nature of these valence band holes is still an open question. Various mechanisms have been suggested but the microscopic origin of carrier-induced ferromagnetism is still controversial.¹⁶⁻²¹ Therefore, studying the properties of the valence bands in InMnAs is of fundamental importance. Cyclotron resonance (CR) is a powerful tool for determining band parameters, especially in a DMS alloy, whose bandstructure is very sensitive to external magnetic fields. However, in the presence of disorder and scattering by Mn impurities in InMnAs, one needs to employ ultrahigh magnetic fields (50–100 Tesla) where $\omega_c\tau > 1$ in order to observe CR. Megagauss CR studies have been performed on *n*-type CdMnTe²² and *n*- and *p*-type InMnAs²³⁻²⁹ and have shown that the Mn impurities have a significant effect on the electronic structure of DMS alloys.

In this paper, in order to study the electronic and optical properties of DMS alloys theoretically, we employ a modified 8-band Pidgeon-Brown effective

mass Hamiltonian³⁰ which is generalized to include the dependence of the band structure on the wavevector k parallel to \mathbf{B} as well as the *sp-d* exchange interaction between the band electrons and holes with the localized Mn spins.

In Appendix A, we discuss the accuracy of the eight band $\mathbf{k} \cdot \mathbf{p}$ theory for magnetic fields up to 100 T. In Appendix B, we give the details of the effective mass Hamiltonian.

2. Samples

Here we present the study on three p-InMnAs samples with various Mn concentrations ($x = 0.0015, 0.006, 0.025$) and a Be-doped *p*-type InAs structure, all grown by molecular beam epitaxy (MBE). The InMnAs samples were grown at low temperatures.²⁹ The characteristics of the samples are shown in Table 1. The dimensions of the samples for the CR experiment were about $2 \times 2 \text{ mm}^2$. The temperature was controlled from room temperature to 10 K using a liquid-helium flow cryostat.

3. Theory

For NGS such as InMnAs with large non-parabolicity, instead of using the Luttinger model, which only includes the valence bands, employing an 8-band Pidgeon-Brown model,³⁰ which considers both the valence and conduction bands is necessary. The detailed theoretical treatment of InMnAs was described in Ref. 27 where *n*-type DMSs were

Table 1. Characteristics of the In_{1-x}Mn_xAs structures studied in this work. All samples are 1 μm thick. The $x = 0$ sample (InAs) is Be-doped. The sample with $x = 0.025$ has 190 nm of InAs as a buffer layer.

x (%)	Density 10^{19} cm^{-3}	Mobility cm^2/Vs	T_c K	Resistivity ($\text{m}\Omega\text{-cm}$)
0	0.5	N/A		
0.0015	1.1	59	< 4	6.6
0.006	1.8	64	< 4	5.3
0.025	1		< 10	

considered. CR in p -type DMS is more complicated due to the greater complexity of the valence bands. The formalism presented here follows our previous work on n -type systems, and the reader is referred to this reference for details of the effective mass formalism. Here we simply outline some of the important points.

The holes of $\text{In}_x\text{Mn}_{1-x}\text{As}$ in a magnetic field experience three types of interaction which result in Landau and Zeeman splitting, in addition to the sp - d exchange splitting. Thus for the Hamiltonian of the system, we can write:

$$H = H_L + H_Z + H_{Mn}, \quad (1)$$

where explicit expressions for effective mass Hamiltonians, H_L , H_Z and H_{Mn} are given in Ref. 28 and Appendix B.

Following the Pidgeon and Brown formalism, we find it convenient to separate the eight Bloch basis states into an upper set and a lower set which decouple at the zone center, i.e., $k_z = 0$. The Bloch basis states we choose for the upper set are

$$|1\rangle = \left| \frac{1}{2}, +\frac{1}{2} \right\rangle = |S \uparrow\rangle, \quad (2a)$$

$$|2\rangle = \left| \frac{3}{2}, +\frac{3}{2} \right\rangle = \frac{1}{\sqrt{2}}|(X + iY) \uparrow\rangle, \quad (2b)$$

$$|3\rangle = \left| \frac{3}{2}, -\frac{1}{2} \right\rangle = \frac{1}{\sqrt{6}}|(X - iY) \uparrow + 2Z \downarrow\rangle, \quad (2c)$$

$$|4\rangle = \left| \frac{1}{2}, -\frac{1}{2} \right\rangle = \frac{i}{\sqrt{3}}|-(X - iY) \uparrow + Z \downarrow\rangle, \quad (2d)$$

which correspond to electron spin up, heavy-hole (HH) spin up, light-hole (LH) spin down, and split off hole spin down. Likewise, the Bloch basis states for the lower set are

$$|5\rangle = \left| \frac{1}{2}, -\frac{1}{2} \right\rangle = |S \downarrow\rangle, \quad (3a)$$

$$|6\rangle = \left| \frac{3}{2}, -\frac{3}{2} \right\rangle = \frac{i}{\sqrt{2}}|(X - iY) \downarrow\rangle, \quad (3b)$$

$$|7\rangle = \left| \frac{3}{2}, +\frac{1}{2} \right\rangle = \frac{i}{\sqrt{6}}|(X + iY) \downarrow - 2Z \uparrow\rangle, \quad (3c)$$

$$|8\rangle = \left| \frac{1}{2}, +\frac{1}{2} \right\rangle = \frac{1}{\sqrt{3}}|(X + iY) \downarrow + Z \uparrow\rangle, \quad (3d)$$

corresponding to electron spin down, HH spin down, LH spin up, and split off hole spin up.

For the vector potential, we choose the Landau Gauge

$$\mathbf{A} = -By\hat{x}, \quad (4)$$

from which we obtain $\mathbf{B} = \nabla \times \mathbf{A} = B\hat{z}$.

To avoid confusion, we point out that the hole masses are different along the quantization direction parallel to the field (z) and in the x - y plane perpendicular to the field. Our heavy and light hole designation refers to the effective mass in the confinement direction. For cyclotron motion in the plane perpendicular to the field, things are reversed, i.e., ‘‘light’’ holes have the heavier cyclotron mass while ‘‘heavy’’ holes have the lighter cyclotron mass.

With the choice of Landau Gauge (4), translational symmetry in the x direction is broken while translational symmetry along the y and z directions is maintained. Thus k_y and k_z are good quantum numbers and the envelope of the effective mass Hamiltonian (1) can be written as

$$\mathcal{F}_{p,\nu} = \frac{e^{i(k_y y + k_z z)}}{\sqrt{\mathcal{A}}} \begin{bmatrix} a_{1,\nu} \phi_{p-1} \\ a_{2,\nu} \phi_{p-2} \\ a_{3,\nu} \phi_p \\ a_{4,\nu} \phi_p \\ a_{5,\nu} \phi_p \\ a_{6,\nu} \phi_{p+1} \\ a_{7,\nu} \phi_{p-1} \\ a_{8,\nu} \phi_{p-1} \end{bmatrix}. \quad (5)$$

In Eq. (5), as described in Refs. 4, 31 and 32, it is important to note the Pidgeon–Brown manifold number p is not the same thing as the Landau level number, which is the harmonic oscillator number n and varies depending on the component. The relation between the usual Landau quantum number n and the Pidgeon–Brown index p is shown in Table 1 of Ref. 31 for any given basis state. Since the harmonic oscillator functions, $\phi_n(\xi)$, are only defined for $n \geq 0$, it follows from Eq. (5) that $\mathcal{F}_{p,\nu}$ is defined for Pidgeon–Brown index $p \geq -1$. For $p = -1$, we see from Eq. (5) that there is only one nonzero state, corresponding to the 6th component which is the heavy hole spin down state. For $p = 0$ there are four nonzero states and for $p = 1$ there are seven nonzero states. For $p \geq 2$, all eight components are nonzero. Note that for a given Pidgeon–Brown manifold p , there are several different Landau levels present. For

example, if the Pidgeon–Brown manifold number $p = 2$, the first component (conduction-band up state) is in the $n = 1$ Landau level while the second component (HH up state) is in the $n = 0$ Landau level. Keeping track of the Pidgeon–Brown manifold number allows us to more easily identify the different transitions. The index ν labels the eigenvectors in order of increasing energy, $\mathcal{A} = L_x L_y$ is the cross sectional area of the sample in the x - y plane, $a_{i,\nu}(k_z)$ are complex expansion coefficients for the ν th eigenstate which depend explicitly on k_z , and $\phi_n(\xi)$ are harmonic oscillator eigenfunctions evaluated at $\xi = x - \lambda^2 k_y$. We label our states using the following notation: (p, ν) , where p is the Pidgeon–Brown manifold index which starts from -1 , and ν is the energy level (ordered from lowest to highest) within that Pidgeon–Brown manifold. As discussed above, the maximum value of ν is 8 for $p \geq 2$ but is 1, 4, and 7 for $p = -1, 0$, and 1 respectively.

The magnetic length, λ , is

$$\lambda = \sqrt{\frac{\hbar c}{eB}} = \sqrt{\frac{\hbar^2}{2m_0} \frac{1}{\mu_B B}}, \quad (6)$$

where $\mu_B = 5.789 \times 10^{-5}$ eV/Tesla is the Bohr magneton and m_0 is the free electron mass.

Substituting $\mathcal{F}_{n,\nu}$ from Eq. (5) into the effective mass Schrödinger equation with H given by Eq. (1), we obtain a matrix eigenvalue equation

$$H_p F_{p,\nu} = E_{p,\nu}(k_z) F_{p,\nu}, \quad (7)$$

that can be solved for each allowed value of p , the Pidgeon–Brown index to obtain the energy levels $E_{p,\nu}(k_z)$. The components of normalized eigenvectors, $F_{p,\nu}$, are the expansion coefficients, $a_{i,\nu}$ which in general depend upon k_z . Again, since the harmonic oscillator functions, $\phi_n(\xi)$, are only defined for $n \geq 0$, it follows from Eq. (5) that $F_{p,\nu}$ is defined for $p \geq -1$. In solving the effective mass Schrödinger Eq. (7), rows and columns for which $n < 0$ are deleted in the effective mass Hamiltonian. The energy levels are $E_{p,\nu}(k_z)$ where p labels the Pidgeon–Brown manifold and ν labels the eigenenergies belonging to the same manifold in ascending order.

We solve the above equation in the *axial* approximation. In this approximation, we effectively replace γ_2 and γ_3 by their average, $(\gamma_2 + \gamma_3)/2$ and neglect their difference $\gamma_2 - \gamma_3$. In this approximation, the Pidgeon–Brown manifolds decouple and we can solve each Pidgeon–Brown Hamiltonian H_p

separately. This is described in the Appendix B (see Eq. (B.8e) and the discussion thereafter).

The magneto-optical absorption coefficient for a given photon energy $\hbar\omega$ is given by³³:

$$\alpha(\hbar\omega) = \frac{\hbar\omega}{(\hbar c)n_r} \epsilon_2(\hbar\omega), \quad (8)$$

where $\epsilon_2(\hbar\omega)$ is the imaginary part of the dielectric function and n_r is the index of refraction. The imaginary part of the dielectric function is found using Fermi's golden rule as described in Ref. 28 and the material parameters that we used are listed in Table 1 of Ref. 28.

3.1. Valence subband structure

In our calculations, we assume de-localized p -like holes in the valence bands, and compute the electronic structures and magneto-optical properties in the paramagnetic limit. Solving the effective mass Schrödinger Eq. (7), we obtain the valence subband structure as a function of Mn concentration, x and wavevector, k_z . The valence subband structure of $\text{In}_{1-x}\text{Mn}_x\text{As}$ for $T = 30$ K and $B = 100$ Tesla for $x = 0$ and $x = 2.5\%$, is shown in Fig. 1. Comparing Figs. 1(a) and 1(b), we see that doping with Mn leads to shifts of the valence bands due to the exchange interaction between valence band holes and localized Mn magnetic moments. In this subband structure, the Pidgeon–Brown manifold with $p = -1$ contains only 1 state which is a pure HH spin down state in the $n = 0$ Landau level and is a 1×1 Hamiltonian with a simple parabolic dispersion relation, and labeled as $H_{-1,1}$.

As seen in Fig. 1(b), the most pronounced effect of Mn doping on the computed valence band Landau levels is the reversal in energy of two states, namely the pure heavy hole $H_{-1,1}$ state and the $L_{1,5}$ state which is primarily a LH spin up state near the zone center. These two states are the lowest-lying hole levels in undoped and doped samples, respectively. Therefore in the limit of low carrier density, they will be the only occupied states. Thus, a major effect of Mn doping is to change the spin state of the system through the exchange interaction between the valence band holes and the localized Mn spins.

3.2. CR absorption

Our theoretically computed CR absorption in p -doped InAs (zero Mn concentration), for h-active

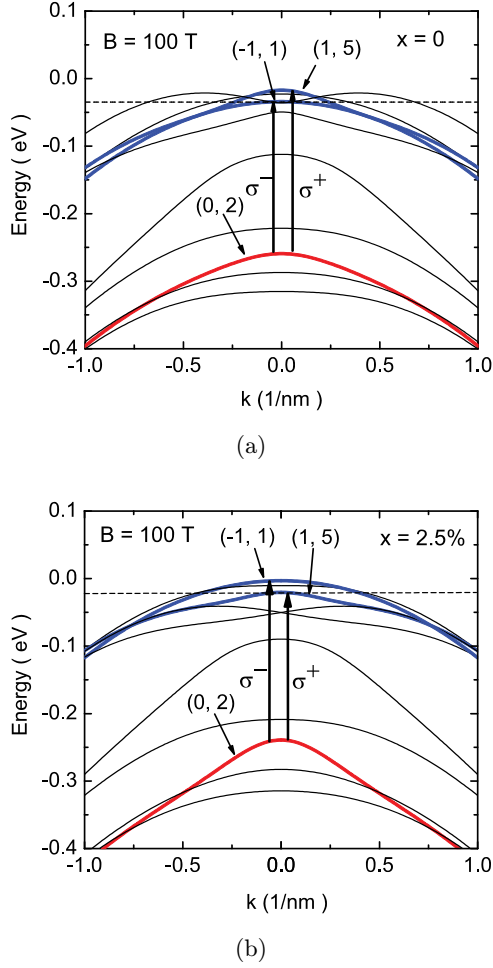


Fig. 1. Valence band structure for $T = 30$ K and $B = 100$ T for $\text{In}_{1-x}\text{Mn}_x\text{As}$ alloys having (a) $x = 0\%$ and (b) $x = 2.5\%$. For $x = 0\%$, the first HH state, $H_{-1,1}$, lies below the LH state $L_{1,5}$. For $x = 2.5\%$, the order of these two states is reversed. Two possible CR transitions are shown using upward arrows, namely a hole-active (h-active) (σ^-) transition between $H_{0,2}$ and $H_{-1,1}$, and an electron-active (σ^+) transition from $H_{0,2}$ to $L_{1,5}$. The dashed lines are the Fermi energies for a hole density of 10^{19} cm^{-3} .

circularly polarized radiation with photon energy $\hbar\omega = 0.117$ eV at $T = 20$ K, is shown in Fig. 2(b) for a hole concentration of $p = 10^{19} \text{ cm}^{-3}$. The CR absorption spectrum is broadened by assuming a Lorentzian-type lineshape with a FWHM linewidth of 4 meV, which is much narrower than in the experimental situation, in order to resolve any closely spaced CR peaks and provide better magnetic field values for the calculated CR peaks.

To better understand the origin of the CR absorption peaks, the Landau levels at $k = 0$ are shown in Fig. 2(a). The Fermi level for $p = 10^{19} \text{ cm}^{-3}$ is indicated by the dashed line in the diagram. At a

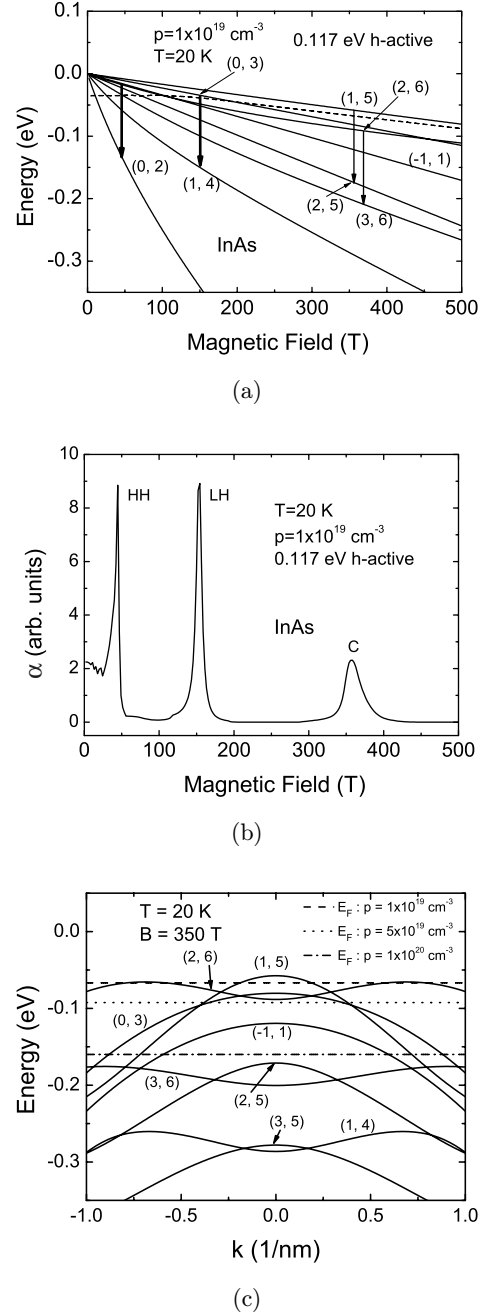


Fig. 2. The upper panel (a) shows the $k = 0$ valence band Landau levels as a function of the magnetic field and the Fermi level for $p = 10^{19} \text{ cm}^{-3}$ (dashed line). The CR absorption in *p*-type InAs is shown in (b) for h-actively polarized radiation with $\hbar\omega = 0.117$ eV at $T = 20$ K and $p = 10^{19} \text{ cm}^{-3}$. To include the broadening, a FWHM linewidth of 4 meV is considered. The k -dependent Landau subband structure at $B = 350$ Tesla is shown in the panel (c).

hole density of 10^{19} cm^{-3} only Landau levels very close to the valence band edge are occupied by holes. The transitions responsible for the strong CR absorption peaks are indicated by the vertical arrows.

Holes excited from the low-lying Landau levels give rise to three CR peaks. The CR absorption peak near 40 Tesla is due to a transition between the Landau subbands $H_{-1,1}$ and $H_{0,2}$. Near the zone center, the $H_{0,2}$ level is primarily HH spin down which accounts for our use of the “H” designation for this subband. The CR peak near 150 Tesla is due to a transition between the $L_{0,3}$ and $L_{1,4}$ states where “L” indicates that the states are primarily of LH characteristic at $k = 0$. We note that the LH transition occurs at a higher magnetic field than the HH transition. While at first this might seem counter-intuitive, it is consistent with the fact that the in-plane mass for the LH is bigger than the in-plane mass for the HH as discussed earlier.

There is another CR absorption peak around 350 Tesla, labeled “C”, which can be resolved into a closely spaced pair of HH and LH peaks indicated by the two vertical arrows in Fig. 2(a), i.e., a LH $L_{1,5}$ to $L_{2,5}$ transition and a HH $H_{2,6}$ to $H_{3,6}$ transition. The $H_{2,6}$ to $H_{3,6}$ transition demands some explanation since it would appear from the fan diagram that both initial and final states are below the Fermi level and contain no holes. So how can there be a CR absorption peak for this transition? The answer can best be seen by plotting the k -dependent Landau level subband structure at 350 Tesla. This is done in Fig. 2(c) where Fermi levels are shown for hole concentrations of $p = 10^{19} \text{ cm}^{-3}$, $5 \times 10^{19} \text{ cm}^{-3}$ and 10^{20} cm^{-3} . The $H_{2,6}$ Landau subband exhibits a camel back structure and at a hole concentration of $p = 10^{19} \text{ cm}^{-3}$ only states near $k = 0.6 \text{ nm}^{-1}$ are occupied while states at the Γ point are empty. It is clear that the $H_{2,6}$ to $H_{3,6}$ transition takes place between states near $k = 0.6 \text{ nm}^{-1}$. As an aside, our analysis reveals that the transition at the Γ point between the two states is actually forbidden while mixing of states away from the Γ point gives rise to non-vanishing optical matrix elements.

Finally, we should note that for $B < 30$ Tesla, higher-order Landau levels become occupied and excitations of holes from these subbands are responsible for the downward sloping plateau seen in the CR absorption in Fig. 2(b) for $B < 30$ T.

Our experimental observations show that the h-active CR peak positions in $\text{In}_{1-x}\text{Mn}_x\text{As}$ are surprisingly insensitive to x . In Fig. 3, we plot the lowest lying HH, LH, and “C” CR peak positions as functions of magnetic field in four samples having Mn concentrations ranging from $x = 0$ to $x = 0.025$ with different excitation photon energies. The solid

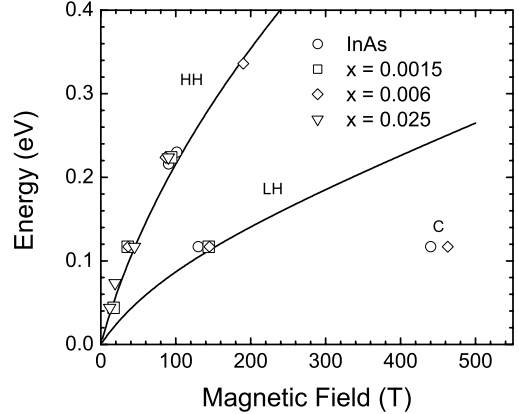


Fig. 3. Observed h-active CR peak positions for the HH, LH and “C” features for four samples with different Mn concentrations. The two solid curves are calculated peak positions based on the 8-band effective mass model described in the text.

curves are the theoretically computed CR peak positions for the HH and LH CR transitions for InAs, in the paramagnetic limit. However, by inspecting Fig. 1, we see that band structures are strongly affected by Mn doping. It is possible that the band structure changes are not evidently revealed by the CR peak position shifts, since the initial and final states involved in a transition may shift together in energy and thus the CR peak position does not change significantly. Thus, the alteration of the band structure induced by doping with Mn concentrations is not necessarily manifested by only h-active CR spectra.

While the h-active CR peak positions may be insensitive to the Mn concentration, the CR spectra depend sensitively on the hole density due to Fermi filling effects. Figure 4 shows theoretical h-active CR absorption spectra in $\text{In}_{0.975}\text{Mn}_{0.025}\text{As}$ for photon energies having $\hbar\omega = 0.224 \text{ eV}$. We plot the CR absorption at two different hole concentrations, $p = 2 \times 10^{18} \text{ cm}^{-3}$ and $5 \times 10^{18} \text{ cm}^{-3}$ and at three different temperatures, namely $T = 17 \text{ K}$, 46 K and 70 K , assuming a narrow FWHM linewidth of 4 meV .

The CR absorption spectra exhibit asymmetric peaks with a broad tail at low fields. Note that the width of the low field tail depends on the free hole concentration. The curves with a hole density of $5 \times 10^{18} \text{ cm}^{-3}$ have a broad tail at low fields, while the curves with a hole density of $2 \times 10^{18} \text{ cm}^{-3}$ have a narrow tail. At low densities, the absorption is

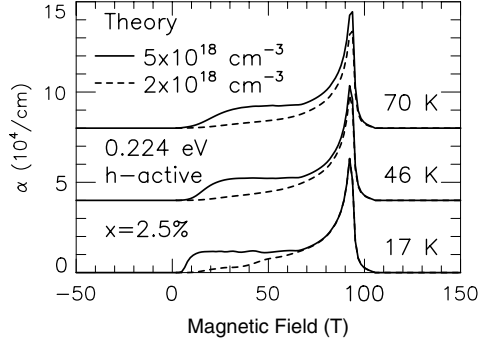
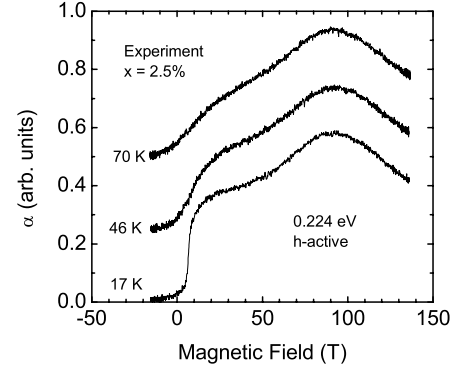


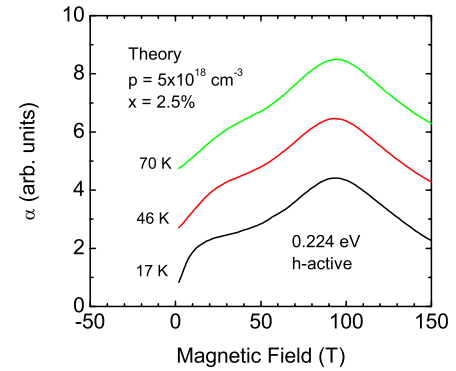
Fig. 4. CR dependence on hole densities. Due to the Fermi filling effect, the CR spectrum with higher hole density has a plateau at low fields, which becomes smoother with increasing temperature.

primarily due to one transition, the heavy-hole transition. The asymmetry in the line-shape comes from the fact that the sample is 3D, and as a result, k_z is still a good quantum number. The absorption peak occurs near $k_z = 0$ but can also occur slightly away from $k_z = 0$ and this gives rise to the asymmetry of the line-shape. At higher densities, the extra width of the low field tail results from the population of higher-order Landau levels (see Fig. 2(a) for low fields, where at high carrier densities, many more Landau levels become unpopulated leading to more CR transitions). The sharpness of the low field cutoff at low temperature is attributed to the sharpness of the Fermi distribution at low temperatures. The HH to HH transition will take place even if the hole density is low, because the $H_{-1,1}$ state is very close to the valence band edge and is almost always occupied, partially or fully. The higher-order transitions need higher free hole densities to have their corresponding levels occupied.

Due to the non-parabolicity of the valence subbands, most CR spectra are generally not symmetric. The asymmetry of the CR absorption curves in Fig. 4 is seen very clearly. Changes in temperature can also bring about changes in the spectral line-shape due to Fermi level sharpening at low temperatures. This can be seen in the experimental data shown in Fig. 5(a) where the 17 K curve has an abrupt cutoff at low magnetic fields. Figure 5(b) shows the results of our theoretical CR absorption spectra, in which the broadening of the CR absorption curves is based on the experimental hole mobilities, which result in FWHM linewidth around 100 meV.



(a)



(b)

Fig. 5. Experimental CR (a) and corresponding theoretical simulations (b). The low temperature CR has an abrupt cutoff at low fields due to the Fermi level sharpening effect.

3.3. Sensitivity of CR energies to material parameters

The material parameters used in the effective mass Hamiltonian can drastically change the valence band structure and the resulting CR absorption spectra. Figures 6 and 7 show the HH and LH CR energy shift in $\text{In}_{1-x}\text{Mn}_x\text{As}$ with respect to the relative change in a number of material parameters. We denote this shift in the CR energy by $\delta E_{\text{CR}}/(\delta\Gamma/\Gamma)$. The material parameters Γ include the Luttinger parameters $\gamma_1, \gamma_2, \gamma_3$, Kane's parameter E_p , and the effective electron mass m_e^* . Shifts in the CR photon energy are plotted as a function of the resonance field. It should be remarked that the resonance photon energy is not constant but varies with the magnetic field. As expected, shifts in the CR photon energy vanish if the resonance field vanishes. In all cases the temperature is taken to be 30 K and results are plotted for Mn concentrations of 0% and 5%.

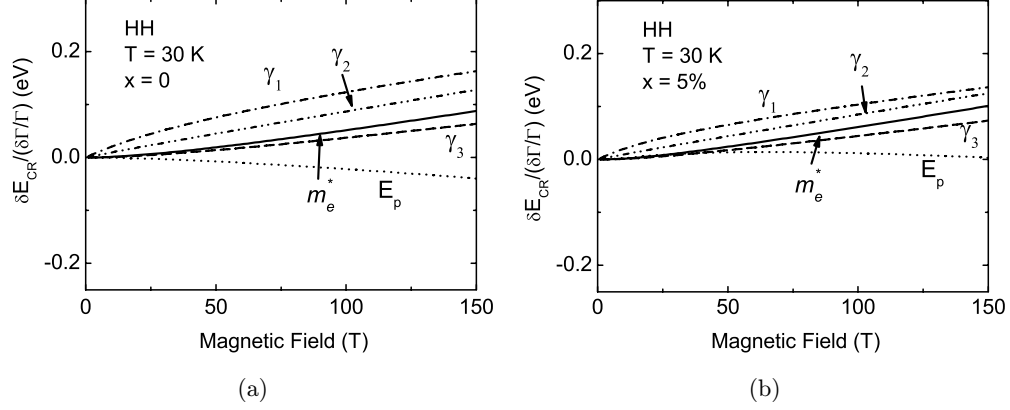


Fig. 6. The HH CR energy dependence on material parameters Γ in $\text{In}_{1-x}\text{Mn}_x\text{As}$ as a function of the magnetic field at $T = 30$ K. (a) is for $x = 0\%$ and (b) is for $x = 5\%$.

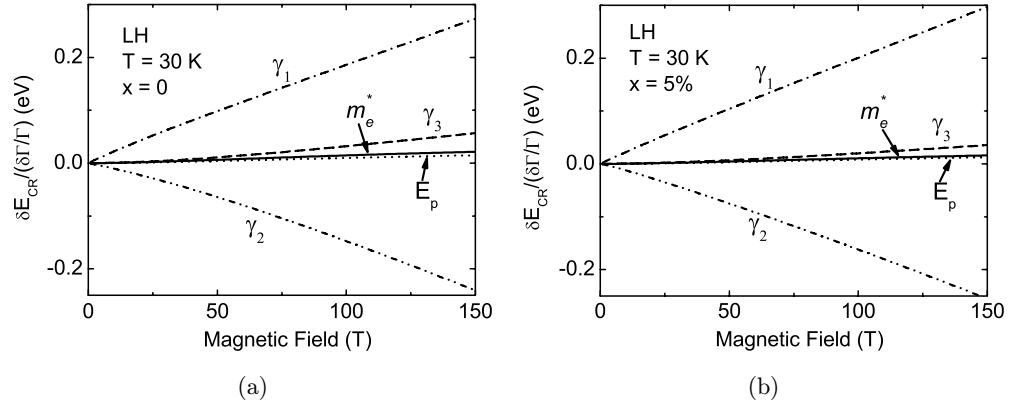


Fig. 7. The LH CR energy dependence on material parameters Γ in $\text{In}_{1-x}\text{Mn}_x\text{As}$ as a function of the magnetic field at $T = 30$ K. (a) is for $x = 0\%$ and (b) is for $x = 5\%$.

Comparing Figs. 6(a) and 7(a) we find that the LH transition in InAs is more sensitive to small changes in the material parameters than the HH transitions. For instance, a 10% change in γ_1 will result in a ~ 25 meV change at $B = 140$ T in the LH CR energy, which in turn will result in about a 50 T CR position shift in the resonance field when the photon energy is 0.117 eV. In Figs. 6(b) and 7(b) the sensitivity of the CR energy to changes in the material parameters in $\text{In}_{0.95}\text{Mn}_{0.05}\text{As}$ are plotted. We find that 5% Mn doping does not strongly alter the sensitivity to small changes in the material parameters.

It is instructive to demonstrate how the CR absorption depends on the valence band Luttinger parameters. The nominal values of the Luttinger parameters in InAs are $\gamma_1 = 20$, $\gamma_2 = 8.5$ and $\gamma_3 = 9.2$.³⁴ In Fig. 8, we plot theoretical CR

absorption spectra in InAs for three different sets of Luttinger parameters while fixing all other material parameters at their nominal values. The bottom curve in Fig. 8 is based on the nominal InAs Luttinger parameters. The upper curve illustrates what happens when γ_1 is increased by 5% and the middle curve shows what happens when γ_3 is increased by 5%. In all three simulations, we assume that the temperature $T = 30$ K and that the hole concentration $p = 10^{19} \text{ cm}^{-3}$. From Fig. 8 it is clear that the HH CR peak near 40 Tesla is relatively insensitive to small changes in the Luttinger parameters while the position and shape of the LH CR feature near 150 Tesla is very sensitive to changes in the Luttinger parameters. Due to the sensitive dependence of the CR spectra on the material parameters, it may furnish an effective way to refine these parameters.

3.4. Selection rules, valence band mixing and e-active CR in *p*-type semiconductors

Selection rules for CR are a direct result of the conservation of energy and angular momentum. For a free electron or a hole system (that is, ignoring the crystal potential), CR can only be observed for a specific circular polarization. For instance, in a free electron system, CR transitions occur for σ^+ circular polarization while for a free hole system, CR occurs only for σ^- circular polarization. As a result, CR in σ^+ polarization is often called e-active and σ^- polarization is referred to as h-active. Recently, we have experimentally observed e-active CR in *p*-doped InAs and InMnAs. The temperature was quite low (12 K) and the hole concentration was high enough (10^{19} cm^{-3}) to safely eliminate the possibility that the e-active CR comes from the thermally excited electrons in the conduction band. Since it is also known that p-InSb and p-InAs can have a 2DEG on the surface of the structures, it is possible that the e-active absorption can come from the surface carriers. However, the results from our theoretical model suggest that e-active absorption in the *p*-doped system comes from having two types of holes (heavy and light) with different M_j quantum numbers. With a full treatment of the semiconductor energy band structure within our modified Pidgeon–Brown model, it is easy to explain the e-active CR results in terms of the degeneracy of the valence

band states. Specifically, having multiple valence band states (HH: $J = 3/2$, $M_j = \pm 3/2$; LH: $J = 3/2$, $M_j = \pm 1/2$) allows one to simultaneously satisfy conservation of angular momentum and energy in cyclotron absorption for both σ^+ and σ^- polarizations. Note that this is not a consequence of valence band mixing between the HH and LH states (though mixing between the conduction and valence bands is needed to pick up oscillator strength for the transitions). It is simply required to have degenerate valence band states with differing M_j quantum numbers. We note that some people might not think of this as “true” CR since it involves a change in the species of the holes. Nevertheless, it corresponds to absorption between the valence band Landau levels for electron-active circularly polarized light.

The effective mass wave function is a product of the rapidly oscillating periodic part of the Bloch basis functions at the zone center u_i and the slowly varying envelope function $\mathcal{F}_{p,\nu}$,

$$\Psi_{p,\nu} = \sum_{i=1,8} [\mathcal{F}_{p,\nu}]_i u_i, \quad (9)$$

where p is the Pidgeon–Brown manifold number, ν is the ν th energy state within the manifold and $[\mathcal{F}_{p,\nu}]_i$ is the i th component of the envelope function given by Eq. (5). (For the $p = -1, 0$, and 1 manifolds, one sums only over the nonzero components.) The optical matrix elements for e-active and h-active polarizations are given by:

$$\langle \Psi_{p',\nu'} | \hat{P}_{\pm} | \Psi_{p,\nu} \rangle. \quad (10)$$

The matrix element splits into two parts, an *intraband* and an *interband* part. For CR, one is normally interested in the intraband term, but in narrow gap materials, strong band mixing gives a substantial contribution to the interband term which can dominate.³⁵ One can substitute the wave function in Eq. (9) into Eq. (10) and then determine the selection rules for optical transitions. However, since we have made the *axial* approximation discussed above, the different Pidgeon–Brown manifolds decouple and it is easy to determine the selection rules. We see that from Eq. (5) that within a given Pidgeon–Brown manifold p , there are several different values for the harmonic oscillator states for the different components (i.e., the components are in different Landau levels). While within a given manifold, the oscillator states differ for the components, we note that the sum of the

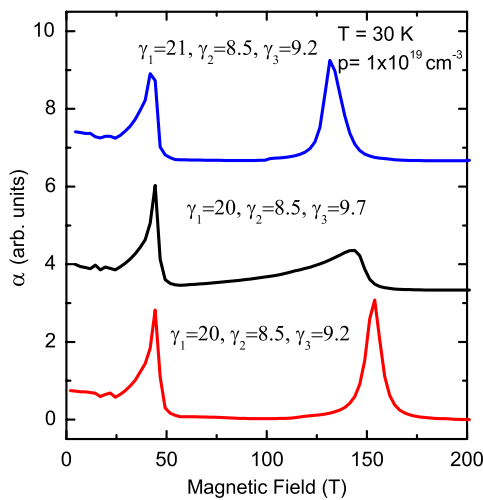


Fig. 8. Theoretical CR spectra of InAs using three different sets of Luttinger parameters. The bottom curve is obtained using nominal values of the Luttinger parameters. The LH transition is seen to be more sensitive to small changes in the Luttinger parameters.

Landau Level number n and the m_j quantum number of the corresponding Bloch state are the same for all components. In fact, we see that $n + m_j = p - 1/2$ for all components of the manifold. Since in the axial approximation, the different Pidgeon–Brown manifolds do not couple, it is easy to see that the selection rules for optical transitions in e-active and h-active polarizations are obtained from

$$\langle \Psi_{p',\nu} | \hat{P}_{\pm} | \Psi_{p,\nu} \rangle \propto \delta_{p',p\pm 1}. \quad (11)$$

As a result of the selection rules, we see that σ^+ illumination leads to transitions which increase the manifold quantum number by one ($p \rightarrow p + 1$) while σ^- leads to transitions which decrease the manifold quantum number by one ($p \rightarrow p - 1$).

In the conduction band, increasing the manifold quantum number always increases the energy. As a result, only transitions with increasing p (and therefore also the Landau level index n) may take place in absorption, therefore only e-active (σ^+) CR can be observed in the conduction band.

The valence band, however, consists of two types of carriers: HHs ($J = 3/2, M_j = \pm 3/2$) and LHs ($J = 3/2, M_j = \pm 1/2$). Each of them has their own Landau ladder in a magnetic field. An increase of n always implies a decrease in energy *but only within each ladder*. Like the conduction band case, transitions within a ladder (HH \rightarrow HH or LH \rightarrow LH) can take place only in h-active (σ^-) polarization. However, the relative position of the two ladders can be such that interladder transitions (LH \rightarrow HH) in e-active polarization are allowed. This process is schematically shown in Fig. 9. Note that this figure

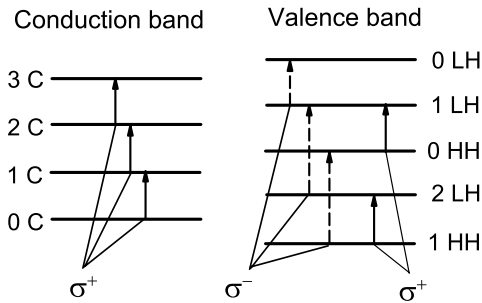


Fig. 9. Schematic diagram of Landau levels and CR transitions in conduction and valence bands. Both h-active and e-active transitions are allowed in the valence band because of the degenerate valence band structure. Only e-active transitions are allowed in the conduction band.

is extremely simplified and should be used only as a qualitative explanation of the effect.

We have examined e-active CR at a photon energy of 0.224 eV in p -type InAs at $T = 12$ K with a delocalized hole density of 10^{19} cm^{-3} . In Fig. 10(a), a fan diagram consisting of the computed $k = 0$ valence band energies is plotted as a function of the magnetic field. The field-dependent Fermi level is shown as a nearly horizontal dashed line and the three strongest e-active CR transitions are indicated by vertical arrows whose relative thicknesses correspond to the strengths of the three CR absorption transitions. The corresponding e-active CR absorption spectra is shown in Fig. 10(b). The most pronounced e-active transition near 95 Tesla is the sharp interladder transition $H_{0,2} \rightarrow L_{1,5}$. Another strong interladder transition $H_{1,3} \rightarrow L_{2,6}$ is seen

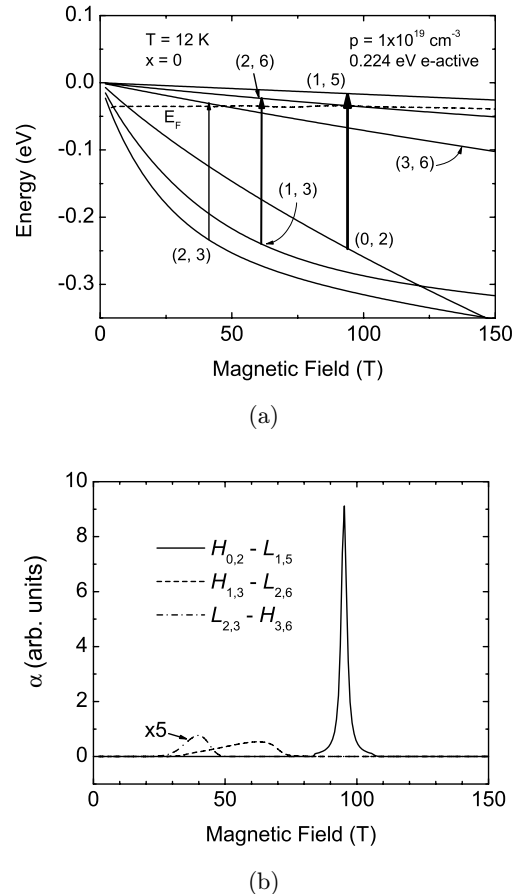


Fig. 10. The Landau level fan diagram (a) and the three strongest e-active CR features at a photon energy of 0.224 eV (b) in p -type InAs as a function of the magnetic field. The temperature is $T = 12$ K and the free hole concentration is $p = 10^{19} \text{ cm}^{-3}$. In (a) the Fermi level is indicated by the dashed line.

near 60 Tesla. This interladder transition has a large oscillator strength but is broader by virtue of the high degree of nonparabolicity in the valence bands. There are some other less pronounced transitions, which contribute to absorption spectra at lower fields.

We now consider the effects of Mn doping on the computed e-active CR absorption spectra in Fig. 10. We assume that the samples remain paramagnetic in the presence of Mn doping. In Sec. 3.1, the Mn doping effect on the valence band structure of $\text{In}_{1-x}\text{Mn}_x\text{As}$ was briefly addressed. It was noted that with the Mn doping, the subband structure is greatly altered, and thus the CR spectra can be changed. The most pronounced effect is the shift of the first HH state $H_{-1,1}$ to the top of the valence band and the shift of the LH state $L_{1,5}$ to a lower position. The strongest e-active CR peak, which is due to the transition of electrons from the $H_{0,2}$ state to $L_{1,5}$ state, shall also be shifted. Doping with Mn impurities on the other hand will greatly enhance carrier scattering thus increasing the line width and reducing the strength of the CR absorption.

The shift of the e-active $H_{0,2} \rightarrow L_{1,5}$ CR transition is illustrated in Fig. 11. Two e-active CR absorption peaks are plotted for two different values of the Mn concentration, namely $x = 0\%$ and $x = 2.5\%$. The strong e-active transition seen in InAs (solid line) in the absence of Mn doping has been discussed previously and is also shown in Fig. 10. The e-active CR absorption peak in $\text{In}_{0.975}\text{Mn}_{0.025}\text{As}$ (dashed line) is shifted relative to the corresponding

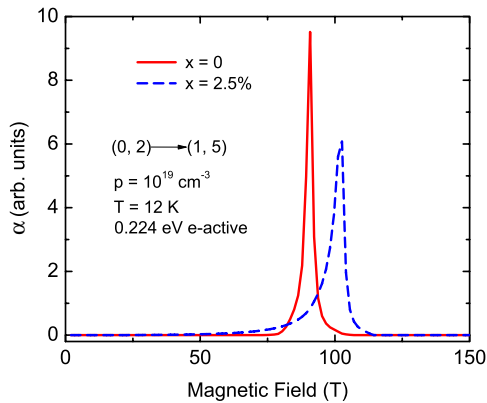


Fig. 11. The e-active CR transition $H_{0,2} \rightarrow L_{1,5}$ in *p*-type $\text{In}_{1-x}\text{Mn}_x\text{As}$ as a function of the magnetic field for $x = 0\%$ (solid line) and $x = 2.5\%$ (dashed line). The temperature is $T = 12$ K, the delocalized hole concentration is $p = 10^{19} \text{ cm}^{-3}$, and the sample is assumed to be paramagnetic.

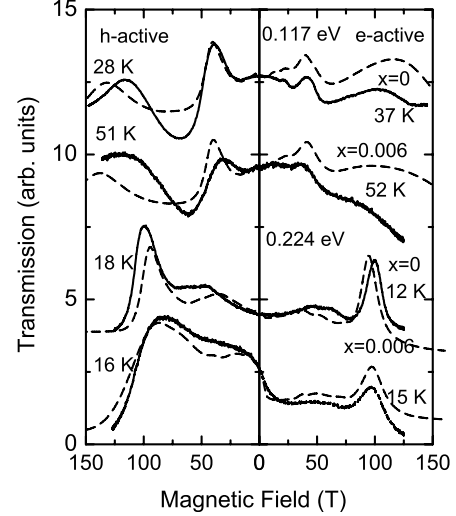


Fig. 12. Experimental and theoretical CR absorption. Solid lines are experimental CR spectra as a function of magnetic field for h-active and e-active polarizations. Corresponding theoretical calculations are shown in dashed lines.

InAs feature to higher fields and has a broad tail at lower fields. The shift is due to the reduced splitting between $H_{0,2}$ and $L_{1,5}$ state as shown in Fig. 1. The tail at lower fields results from the change in the non-parabolic Landau level subband structure, brought about by the exchange interaction.

We have performed CR transmission measurements on bulk $\text{In}_{1-x}\text{Mn}_x\text{As}$ samples with Mn concentrations $x = 0\%$ and $x = 0.6\%$ at several temperatures. In all cases, the samples were found to be in the paramagnetic phase. The calculated and the experimental CR transmission spectra are shown in Fig. 12 for both e-active (right panel) and h-active (left panel) polarizations. As seen in Fig. 12, there is good agreement between theory and experiment. As discussed above, the e-active CR absorption is determined by the $HH \rightarrow LH$ transitions. The main contribution to the h-active CR absorption (left panel in Fig. 12) comes from the transitions within the HH ladder. Using both h- and e-active CR in *p*-type DMSs, it becomes possible to fully characterize the complicated valence band structures in these important materials.

4. Conclusion

We have presented a theoretical and experimental study of the electronic and magneto-optical properties of *p*-type paramagnetic $\text{In}_{1-x}\text{Mn}_x\text{As}$ DMS

alloys in ultrahigh magnetic fields oriented along [001]. We used an 8-band Pidgeon–Brown model generalized to include the wave vector dependence of the electronic states along k_z as well as the s – d and p – d exchange interactions with the localized Mn d electrons. The average Mn spin is treated under the mean field theory framework.

In the case of p -type InMnAs we find that: (i) Mn doping changes the spin states of the DMS system. We find that Mn doping shifts the HH spin down state $H_{-1,1}$ to the valence band edge which, in the absence of doping, is a LH spin up state $L_{1,5}$. The spins of the valence band holes are thereby flipped through the exchange interaction with the localized Mn moments. (ii) Two primary CR absorption peaks are present for magnetic fields up to 300 Tesla for h-active polarization with a photon energy of 0.117 eV. These peaks correspond to $HH \rightarrow HH$ and $LH \rightarrow LH$ transitions. (iii) CR transitions take place not only at the zone center, but also in the regions away from the Γ point. The camel back structures in some of the Landau subbands enhance this effect. (iv) E-active CR absorption in p -type InMnAs is observed and arises due to the complexity of the valence bands. These transitions are seen to arise from transitions between *different* hole ladders ($HH \rightarrow LH$ or $LH \rightarrow HH$). Because h-active CR takes place in the same ladder, both e-active CR and h-active CR can be used to explore the complex valence bands.

In calculating the valence band structure and CR absorption, we find that valence band structure and CR absorption strongly depends on the material parameters. The LH transitions are more affected by changes in the values of these parameters than the HH transitions. This approach can be used as a method to evaluate these parameters. The CR spectra strongly depends on hole densities through the dependence on the Fermi energy in the valence bands. This can also be used to estimate the hole densities, which becomes more meaningful due to the difficulty in traditional methods to measure the carrier densities in the presence of the anomalous Hall effect.

Acknowledgments

This work was supported by the National Science Foundation through Grants DMR-1105437 and DMR-0846834 Career Award.

Appendix A. Validity of 8-Band $\mathbf{k} \cdot \mathbf{p}$ Calculations in High Magnetic Fields

An important question which arises is “How accurate is an 8-band $\mathbf{k} \cdot \mathbf{p}$ model for magnetic fields that are 100 T or more?” One can make a simple estimate for the accuracy of the 8-band $\mathbf{k} \cdot \mathbf{p}$ model. The presence of a magnetic field in the \hat{z} direction quantizes the carrier orbits in the x – y plane. These quantized orbits are approximately given by

$$\frac{\hbar^2}{2m^*}(k_x^2 + k_y^2) = \left(n + \frac{1}{2}\right)\hbar\omega_c \quad (\text{A.1})$$

where $\omega_c = eB/m^*c$ is the cyclotron frequency. Factoring out the effective mass we obtain

$$\frac{\hbar^2}{2}(k_x^2 + k_y^2) = \left(n + \frac{1}{2}\right)\frac{\hbar eB}{c}. \quad (\text{A.2})$$

Note that this is essentially equivalent to the Bohr–Sommerfeld quantization conditions for circular orbits as described in Kittel.³⁶

The maximum value for k_x on an orbit occurs when $k_y = 0$. When this occurs, the magnetic field is related to k_x by:

$$B = \frac{\hbar k_x^2 c}{(2n + 1)e}. \quad (\text{A.3})$$

While this is a simplified model (the hole orbits are not circular but have a complex shape due to warping of the bands), it allows us to estimate for what magnetic fields the 8-band $\mathbf{k} \cdot \mathbf{p}$ theory is valid.

In Fig. A.1 we plot the conduction bands as calculated by both 8-band (solid line) and *full-zone* 30-band (dashed line) $\mathbf{k} \cdot \mathbf{p}$ calculations.^{37–39} Also plotted is the empirical expression for a nonparabolic conduction band (dotted line)

$$\varepsilon(1 + \alpha\varepsilon) = \frac{\hbar^2 k^2}{2m^*}, \quad (\text{A.4})$$

where α is the nonparabolicity parameter. As can be seen, the agreement between the 30-band full-zone calculation and the 8-band model is very good up to about 15–20% of the X and L points at the Brillouin zone boundary.

In Fig. A.2, we see the three valences bands plotted for both the 8-band model (solid lines) and the full-zone 30-band model (dashed lines). Here the agreement is not as good as the conduction band with the 8-band model, agreeing with the full-zone model only to about 10–15% of the zone boundary.

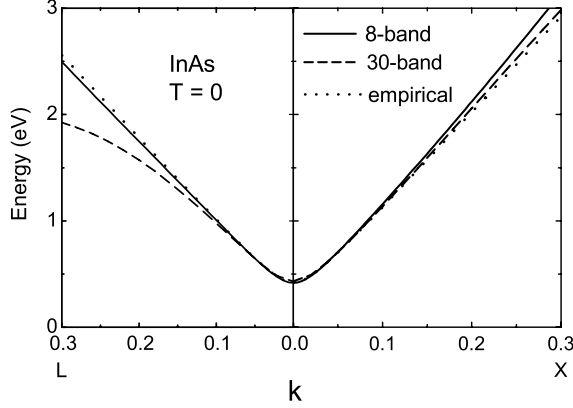


Fig. A.1. The conduction band electronic structure in the X and L directions for different calculations. The solid line is based on 8-band $\mathbf{k} \cdot \mathbf{P}$, the dashed line is for full-zone, 30-band $\mathbf{k} \cdot \mathbf{P}$ theory and the dotted line is based on the empirical nonparabolic formula given by Eq. A.3. As can be seen, the 8-band model accurately models the full zone structure up to about 20% of the zone boundary.

(Note that we have not tried to optimize the parameters of the 30-band model to produce maximum agreement.)

Since the CR transitions involve the $n = 1 \rightarrow n = 0$ transition, we would expect that the 8-band model would be valid up to magnetic fields given by Eq. (A.3) with $n = 1$ and $k_x = 0.1$ to $0.15 k_{zb}$ where $k_{zb} = 2\pi/a$ is the zone boundary wavevector in the \hat{x} direction and a is the lattice constant, for InAs, the lattice constant is 6.06 \AA .

Substituting into Eq. (A.3), we see that if the 8-band model gives agreement with the full zone for 10% of the zone boundary, then the maximum magnetic field is about 234 T. For 15%, the maximum field is 520 T, and for 20% the field is 930 T.

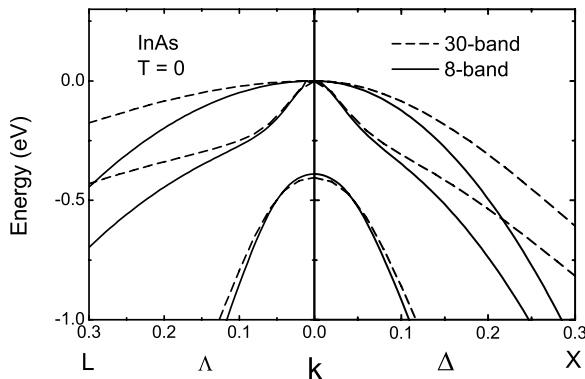


Fig. A.2. Heavy, light and spin-split valence bands for InAs out to 30% of the zone boundary. The 8-band model (solid line) is compared to the full-zone model (dashed line) and shows agreement out to 10–15% of the zone boundary.

These are rather large fields so it is not surprising that good agreement is reached for both the HH transitions (at $\sim 50 \text{ T}$) and the LH transitions (at $\sim 150 \text{ T}$). The higher-order transitions occurring at around 400 T in the experimental data, do not agree as well with the theoretical calculations and might be attributed to the breakdown in the 8-band model.

Appendix B. Effective Mass Hamiltonian

In this appendix, we present explicit expressions for the three effective mass Hamiltonians appearing in Eq. (1) in the basis of the upper and lower set Bloch functions given explicitly in Eqs. (2) and (3).

The effective mass Hamiltonian in bulk zinc blende materials is given in Ref. 40. In the presence of a uniform magnetic field B oriented along the z -axis, the wave vector, \mathbf{k} , is replaced by the operator

$$\mathbf{k} = \frac{1}{\hbar} \left(\vec{p} + \frac{e}{c} \mathbf{A} \right), \quad (\text{B.1})$$

where $\mathbf{p} = -i\hbar\nabla$ is the momentum operator and \mathbf{A} is the Landau gauge vector potential in Eq. (4).

We use creation and destruction operators

$$a^\dagger = \frac{\lambda}{\sqrt{2}} (k_x + ik_y), \quad (\text{B.2a})$$

and

$$a = \frac{\lambda}{\sqrt{2}} (k_x - ik_y), \quad (\text{B.2b})$$

where λ is the magnetic length defined in Eq. (6), to eliminate the operators k_x and k_y , and obtain the Landau Hamiltonian

$$H_L = \begin{bmatrix} L_a & L_c \\ L_c^\dagger & L_b \end{bmatrix} \quad (\text{B.3})$$

with the submatrices L_a , L_b and L_c given by

$$L_a = \begin{bmatrix} E_g + A & i\frac{V}{\lambda} a^\dagger & i\sqrt{\frac{1}{3}} \frac{V}{\lambda} a & \sqrt{\frac{2}{3}} \frac{V}{\lambda} a \\ -i\frac{V}{\lambda} a & -P - Q & -M & i\sqrt{2}M \\ -i\sqrt{\frac{1}{3}} \frac{V}{\lambda} a^\dagger & -M^\dagger & -P + Q & i\sqrt{2}Q \\ \sqrt{\frac{2}{3}} \frac{V}{\lambda} a^\dagger & -i\sqrt{2}M^\dagger & -i\sqrt{2}Q & -P - \Delta \end{bmatrix} \quad (\text{B.4})$$

$$L_b = \begin{bmatrix} E_g + A & -\frac{V}{\lambda}a & -\sqrt{\frac{1}{3}}\frac{V}{\lambda}a^\dagger & i\sqrt{\frac{2}{3}}\frac{V}{\lambda}a^\dagger \\ -\frac{V}{\lambda}a^\dagger & -P - Q & -M^\dagger & i\sqrt{2}M^\dagger \\ -\sqrt{\frac{1}{3}}\frac{V}{\lambda}a & -M & -P + Q & i\sqrt{2}Q \\ -i\sqrt{\frac{2}{3}}\frac{V}{\lambda}a & -i\sqrt{2}M & -i\sqrt{2}Q & -P - \Delta \end{bmatrix} \quad (\text{B.5})$$

$$L_c = \begin{bmatrix} 0 & 0 & \sqrt{\frac{2}{3}}Vk_z & i\sqrt{\frac{1}{3}}Vk_z \\ 0 & 0 & -L & -i\sqrt{\frac{1}{2}}L \\ -i\sqrt{\frac{2}{3}}Vk_z & L & 0 & i\sqrt{\frac{3}{2}}L^\dagger \\ -\sqrt{\frac{1}{3}}Vk_z & -i\sqrt{\frac{1}{2}}L & i\sqrt{\frac{3}{2}}L^\dagger & 0 \end{bmatrix} \quad (\text{B.6})$$

In Eq. (B.3), E_g is the bulk band gap, and Δ is the spin-orbit splitting. The Kane momentum matrix element $V = -\frac{i}{\hbar}\langle S|p_x|X\rangle$ is related to the optical matrix parameter, E_p , by³⁴

$$V = \sqrt{\frac{\hbar^2}{m_0} \frac{E_p}{2}}. \quad (\text{B.7})$$

The operators A , P , Q , L and M are

$$A = \frac{\hbar^2}{m_0} \frac{\gamma_4}{2} \left(\frac{2N+1}{\lambda^2} + k_z^2 \right), \quad (\text{B.8a})$$

$$P = \frac{\hbar^2}{m_0} \frac{\gamma_1}{2} \left(\frac{2N+1}{\lambda^2} + k_z^2 \right), \quad (\text{B.8b})$$

$$Q = \frac{\hbar^2}{m_0} \frac{\gamma_2}{2} \left(\frac{2N+1}{\lambda^2} - 2k_z^2 \right), \quad (\text{B.8c})$$

$$L = \frac{\hbar^2}{m_0} \gamma_3 \left(\frac{-i\sqrt{6} k_z a}{\lambda} \right) \quad (\text{B.8d})$$

and

$$M = \frac{\hbar^2}{m_0} \left(\frac{\gamma_2 + \gamma_3}{2} \right) \left(\frac{\sqrt{3}}{\lambda^2} a^2 \right). \quad (\text{B.8e})$$

In Eq. (B.8e), we have neglected a second term in M proportional to $(\gamma_2 - \gamma_3)(a^\dagger)^2$. We do this for two

reasons: (1) $(\gamma_2 - \gamma_3)$ is small and (2) this term will couple different Landau manifolds making it more difficult to diagonalize the Hamiltonian. The effect of this term can be accounted for later by perturbation theory.

In Eq. (B.8), the number operator $N = a^\dagger a$. The parameters γ_1 , γ_2 and γ_3 used here are not the usual Luttinger parameters since this is an 8-band model, but instead are related to the usual Luttinger parameters γ_1^L , γ_2^L and γ_3^L through the relations⁴¹

$$\gamma_1 = \gamma_1^L - \frac{E_p}{3E_g}, \quad (\text{B.9})$$

$$\gamma_2 = \gamma_2^L - \frac{E_p}{6E_g} \quad (\text{B.10})$$

and

$$\gamma_3 = \gamma_3^L - \frac{E_p}{6E_g}. \quad (\text{B.11})$$

This takes into account the additional coupling of the valence bands to the conduction band not present in the six band Luttinger model.

The parameter γ_4 is related to the conduction band electron effective mass, m_e^* , through the relation⁴⁰

$$\gamma_4 = \frac{1}{m_e^*} - \frac{E_p}{3} \left(\frac{2}{E_g} + \frac{1}{E_g + \Delta} \right). \quad (\text{B.12})$$

The Zeeman Hamiltonian is

$$H_Z = \frac{\hbar^2}{m_0} \frac{1}{\lambda^2} \begin{bmatrix} Z_a & 0 \\ 0 & -Z_a \end{bmatrix}, \quad (\text{B.13})$$

where the 4×4 submatrix Z_a is given by

$$Z_a = \begin{bmatrix} \frac{1}{2} & 0 & 0 & 0 \\ 0 & -\frac{3}{2}\kappa & 0 & 0 \\ 0 & 0 & \frac{1}{2}\kappa & -i\sqrt{\frac{1}{2}}(\kappa+1) \\ 0 & 0 & i\sqrt{\frac{1}{2}}(\kappa+1) & \kappa + \frac{1}{2} \end{bmatrix}. \quad (\text{B.14})$$

The value of κ used in Eq. (B.14) is related to κ^L as defined by Luttinger through the relation⁴¹

$$\kappa = \kappa^L - \frac{E_p}{6E_g}. \quad (\text{B.15})$$

For the Luttinger parameter, κ^L , we use the approximation^{30,42,43}

$$\kappa^L = \gamma_3^L + \frac{2}{3} \gamma_2^L - \frac{1}{3} \gamma_1^L - \frac{2}{3}. \quad (\text{B.16})$$

The exchange interaction between the Mn^{++} d electrons and the conduction s and valence p electrons is treated in the virtual crystal and molecular field approximation. The resulting Mn exchange Hamiltonian is⁴⁴

$$H_{Mn} = x N_0 \langle S_z \rangle \begin{bmatrix} D_a & 0 \\ 0 & -D_a \end{bmatrix}, \quad (\text{B.17})$$

where x is the Mn concentration, N_0 is the number of cation sites in the sample, and $\langle S_z \rangle$ is the average spin on a Mn site. The 4×4 submatrix D_a is

$$D_a = \begin{bmatrix} \frac{1}{2}\alpha & 0 & 0 & 0 \\ 0 & \frac{1}{2}\beta & 0 & 0 \\ 0 & 0 & -\frac{1}{6}\beta & -i\frac{\sqrt{2}}{3}\beta \\ 0 & 0 & i\frac{\sqrt{2}}{3}\beta & \frac{1}{2}\beta \end{bmatrix} \quad (\text{B.18})$$

where α and β are the exchange integrals.

In the paramagnetic phase, the average spin on a Mn site is given in the limit of non-interacting spins by

$$\langle S_z \rangle = -SB_S \left(gS \frac{\mu_B B}{kT} \right), \quad (\text{B.19})$$

where $g = 2$ and $S = \frac{5}{2}$ for the $3d^5$ electrons of the Mn^{++} ion.⁴⁵ The Brillouin function, $B_S(x)$, is defined as

$$B_S(x) = \frac{2S+1}{2S} \coth \left(\frac{2S+1}{2S} x \right) - \frac{1}{2S} \coth \left(\frac{x}{2S} \right). \quad (\text{B.20})$$

The antiparallel orientation of B and $\langle S_z \rangle$ is due to the difference in sign of the magnetic moment and the electron spin. Since B is directed along the z -axis, the average Mn spin saturates at $\langle S_z \rangle = -\frac{5}{2}$.

References

1. G. A. Khodaparast, R. E. Doezema, S. Chung, K. Goldammer and M. B. Santos, *Phys. Rev. B* **70**, 155322 (2004).

2. M. Dobrowolska, K. Tivakornsasithorn, X. Liu, J. K. Furdyna, M. Berciu, K. M. Yu and W. Walukiewicz, *Nature Materials* **11**, 444 (2012).
3. T. Dietl and H. Ohno, *Rev. Modern Phys.* **86**, 187 (2014).
4. G. A. Khodaparast, Y. H. Matsuda, D. Saha, G. D. Sanders, C. J. Stanton, H. Saito, S. Takeyama, T. R. Merritt, C. Feeser, J. F. B. W. Wessels and X. Liu, *Phys. Rev. B* **88**, 235204 (2013).
5. M. Bhowmick, T. Merritt, G. A. Khodaparast, B. W. Wessele, S. A. McGill, D. Saha, X. Pan, G. D. Sanders and C. Stanton, *Phys. Rev. B* **85**, 125313 (2012).
6. H. Munekata, T. Penny and L. L. Chang, *Surf. Sci.* **267**, 342 (1992).
7. H. Ohno, H. Munekata, T. Penney, S. von Molnar and L. L. Chang, *Phys. Rev. Lett.* **68**, 2664 (1992).
8. H. Ohno, A. Shen, F. Matsukura, A. Oiwa, A. Endo, S. Katsumoto and Y. Iye, *Appl. Phys. Lett.* **69**, 363 (1996).
9. F. Matsukura, H. Ohno, A. Shen and Y. Sugawara, *Phys. Rev. B* **57**, R2037 (1998).
10. J. M. Kikkawa and D. D. Awschalom, *Nature (London)* **397**, 139 (1998).
11. Y. Ohno, D. K. Young, B. Beschoten, F. Matsukura, H. Ohno and D. D. Awschalom, *Nature (London)* **402**, 790 (1999).
12. H. Munekata, H. Ohno, R. R. Ruf, R. J. Gambino and L. L. Chang, *J. Cryst. Growth* **111**, 1011 (1991).
13. H. Munekata, A. Zaslavski, P. Fumagalli and R. J. Gambino, *Appl. Phys. Lett.* **63**, 2929 (1993).
14. S. Sanvito, P. Ordejon and N. A. Hill, *Phys. Rev. B* **63**, 165206 (2001).
15. J. König, H. Lin and A. H. MacDonald, *Interacting Electrons in Nanostructures, Lecture Notes in Physics* (Springer, Berlin, 2001).
16. T. Dietl, H. Ohno, F. Matsukura, J. Cibert and D. Ferrand, *Science* **287**, 1019 (2000).
17. J. König, H.-H. Lin and A. H. MacDonald, *Phys. Rev. Lett.* **84**, 5628 (2000).
18. V. I. Litvinov and V. K. Dugaev, *Phys. Rev. Lett.* **86**, 5593 (2001).
19. A. Kaminski and S. D. Sarma, *Phys. Rev. Lett.* **88**, 247202 (2002).
20. G. Zarand and B. Jankó, *Appl. Phys. Lett.* **89**, 047201 (2002).
21. D. E. Angelescu and R. N. Bhatt, *Phys. Rev. B* **65**, 75211 (2002).
22. Y. H. Matsuda, T. Ikaida, M. Miura, S. Kuroda, F. Takano and K. Takita, *Phys. Rev. B* **65**, 115202 (2002).
23. Y. H. Matsuda, T. Ikaida, N. Miura, M. A. Zudov, J. Kono and H. Munekata, *Physica E* **10**, 219 (2001).
24. M. A. Zudov, J. Kono, Y. H. Matsuda, T. Ikaida, N. Miura, H. Munekata, G. D. Sanders, Y. Sun and C. J. Stanton, *Phys. Rev. B* **66**, 161307(R) (2002).

25. G. A. Khodaparast, J. Kono, Y. H. Matsuda, N. Miura, T. Slupinski, A. Oiwa and H. Munekata, *Proc. 26th Int. Conf. Phys. of Semicond.* (2003) p. 320.
26. G. A. Khodaparast et al., *J. Supercond.* **16**, 107 (2003).
27. G. D. Sanders, Y. Sun, C. J. Stanton, G. A. Khodaparast, J. Kono, Y. H. Matsuda, N. Miura, T. Slupinski, A. Oiwa and H. Munekata, *J. Appl. Phys.* **93**, 6897 (2003).
28. G. D. Sanders, Y. Sun, F. V. Kyrychenko, C. J. Stanton, G. A. Khodaparast, M. A. Zudov, J. Kono, Y. H. Matsuda, N. Miura and H. Munekata, *Phys. Rev. B* **68**, 165205 (2003).
29. Y. H. Matsuda et al., *Phys. Rev. B* **70**, 195211 (2004).
30. C. R. Pidgeon and R. N. Brown, *Phys. Rev.* **146**, 575 (1966).
31. R. M. Wood et al., *Phys. Rev. B* **90**, 155317 (2014).
32. E. L. Sesti, D. D. Wheeler, S. E. Hayes, D. Saha, G. D. Sanders and C. J. Stanton, *Phys. Rev. B* **90**, 125301 (2014).
33. F. Bassani and G. P. Parravicini, *Electronic States and Optical Transitions in Solids* (Pergamon, New York, 1975).
34. I. Vurgaftman, J. R. Meyer and L. R. Ram-Mohan, *J. Appl. Phys.* **89**, 5815 (2001).
35. P. Kacman and W. Zawadzki, *Phys. Status Solidi B* **47**, 629 (1971).
36. C. Kittel, *Introduction to Solid State Physics*, 7th edn., John Wiley & Sons, New York, 1996), p. 257 (note that this is equation 30 in Kittel for a spherical orbit).
37. M. Cardona and F. H. Pollak, *Phys. Rev.* **142**, 530 (1966).
38. D. W. Bailey, C. J. Stanton and K. Hess, *Phys. Rev. B* **42**, 3423 (1990).
39. C. J. Stanton, D. W. Bailey and K. Hess *Phys. Rev. Lett.* **65**, 231 (1990).
40. A. L. Efros and M. Rosen, *Phys. Rev. B* **58**, 7120 (1988).
41. J. M. Luttinger, *Phys. Rev.* **102**, 1030 (1956).
42. G. Dresselhaus, A. F. Kip and C. Kittel, *Phys. Rev.* **98**, 368 (1955).
43. G. Dresselhaus, *Phys. Rev.* **100**, 580 (1955).
44. J. Kossut, *Semiconductors Semimetals* **25**, 183 (1988).
45. J. K. Furdyna, *J. Appl. Phys.* **64**, R29 (1988).